Ion-transfer electrochemistry at arrays of nanoscale interfaces between two immiscible electrolyte solutions arranged in hexagonal format

Yang Liu,[1,2] Reza Moshrefi,[3] William D. A. Rickard,[4] Micheál D. Scanlon,[5] T. Jane Stockmann,[3] Damien W. M. Arrigan*,[1]

[1] School of Molecular and Life Sciences, Curtin University, GPO Box U1987, Perth, Western Australia, 6845 Australia
[2] College of Science and Engineering, James Cook University, Townsville, Queensland, 4811 Australia
[3] Memorial University of Newfoundland, Department of Chemistry, 283 Prince Philip Dr., St. John's, Newfoundland, Canada A1B 3X7
[4] John de Laeter Centre, Curtin University, GPO Box U1987, Perth, Western Australia, 6845 Australia
[5] The Bernal Institute and Department of Chemical Sciences, University of Limerick, Limerick V94 T9PX, Ireland

Abstract

The electrochemical behaviour of hexagonally arranged nanopore arrays was studied by simple ion transfer across the interface between two immiscible electrolyte solutions (ITIES) formed between water|1,2-dichloroethane. The hexagonal nanoITIES arrays were supported at nanopores fabricated by focused ion beam milling into 50 nm thick silicon nitride films. Six arrays with different pore centre-to-centre distance (r_c) to radius (r_a) ratios were prepared. Within these arrays, the diffusion-limited steady-state currents (i_{ss}) of tetrapropylammonium cation ($TPrA^+$) ion transfer increased concomitantly with increasing r_c/r_a ratio, reaching a plateau at $r_c/r_a \geq 96$, which is greater than that previously reported for square-patterned nanoITIES arrays ($r_c/r_a \geq 56$). The diffusion regime and i_{ss} associated with simple ion transfer across a nanopore array was also examined using numerical simulations, *via* COMSOL Multiphysics software, incorporating a 3-dimensional geometry and employing finite element analysis. Simulated linear sweep voltammograms of $TPrA^+$ transfer demonstrated a unique diffusional behaviour dependent on hexagonal nanopore spacing and the r_c/r_a ratio, analogous to the experimental voltammograms. Overlay of simulated and experimental voltammograms for each r_c/r_a ratios showed good agreement. These results indicate that a new design criterion is required to achieve independent diffusion at hexagonal nanointerface arrays, in order to maximize nanodevice performance in electrochemical sensor technologies.

1. Introduction

Ion-transfer electrochemistry at the interface between two immiscible electrolyte solutions (ITIES) [1, 2] provides a convenient approach for the detection of ions that are non-redox-active or whose redox-activity has associated complications. This approach has been used for the detection of a wide range of ions and ionisable species [3, 4], including inorganic, organic [5] and biological ions [6, 7] detected *via* simple ion-transfer or facilitated ion-transfer processes. Even when used in stripping analysis mode, which has a preconcentration step that improves sensitivity and lowers detection limits, analytical performance figures of merit are often insufficient for realistic applications such as biomedical or pharmaceutical analysis [8].

Interest in miniaturised ITIES has sought to bring a number of advantages of micro- or nanotechnology to the performance-enhancement of electrochemistry at the ITIES [9]. In addition to a reduction in uncompensated resistance and capacitance, an enhancement in the rate of mass transport can lead to improved electroanalytical performance. Accordingly, micropipettes [10] or microcapillaries [11], and subsequently, nanopipettes [12] prepared by pulled glass pipettes have been explored for the preparation of single micro- or nanoITIES; although, dual-barrelled pipettes can be used to form dual-interface microITIES as well [13]. Concurrently, membranes with arrays of holes or pores of micrometre size were used to modify the ITIES, so as to create an array of microITIES [7]. Fabrication of such membranes were initially achieved by

laser ablation of polymer films [14], subsequently photolithography and reactive ion etching of silicon [15], and more recently laser ablation of glass microscopic coverslips to serve as the interface-modifying membrane [16]. The introduction of membranes with nanopores fabricated by Electron-Beam Lithography (EBL) [17] and Focused Ion Beam (FIB) milling [18] enabled the formation of arrays of nanoITIES [9]. Recently, nanochannels prepared within the micropores of a silicon membrane were proposed to form nanoITIES arrays [19, 20]. The analytical advantages of nanoITIES arrays relative to microITIES arrays putatively include the benefits of efficient mass transport, which is important in the preconcentration step of stripping voltammetry approaches.

The ion-transfer behaviour at miniaturised ITIES arrays is heavily dependent on the array designs, especially the relative locations of adjacent interfaces within the array, and the propensity for diffusion zone formation and extension into adjoining diffusion zones. For microITIES arrays, important design rules were adopted from microelectrode arrays, with typical pore-pore separations (r_c) of more than 20 times the individual pore radius (r_a) to achieve an independent diffusion zone around each pore [21-24]. However, this design rule is not valid for nanoITIES arrays, which might be attributed to the complex mass transport behaviours at nanointerfaces resulting from the comparable size of the depletion layer and Debye length [25, 26]. Godino et al. [27] proposed a design criterion to achieve maximum performance at nanoelectrode arrays, with $r_c \geq 60\ r_a$, which was further experimentally verified by Liu et al. via ion-transfer electrochemistry at nanoITIES arrays [28]. In addition, visualization of ion diffusion provided direct evidence of the significant impact of array design on the behaviour of ion transfer at nanointerface arrays [29].

Design criteria of micro- or nanoarrays are mainly based on the ratio of pore-pore separation distance and the radius (r_c/r_a), thus hexagonal arrangement of interfaces is preferred due to the same separation distance for all pores within the array [17, 30, 31]. In our previous work, the performance of nanoITIES arrays in square arrangement was thoroughly studied to achieve diffusional independence, with $r_c/r_a \geq 56$ [28], which was in good agreement with the simulation results for nanoelectrode arrays [27]. However, the study of mass transport effects at hexagonal arrays is still at an early stage due to the difficulty in fabrication of nanoarrays with variable but well-controlled dimensions.

Analytical solutions to complex and dynamic systems are invaluable for data interpretation and analysis, such as in scanning electrochemical microscopy for probe approach curves [32, 33], Fermi level and electrocatalytic current of nanoparticle films at the ITIES [34], and ionic surfactant adsorption at the ITIES [35]. Meanwhile, advanced computational methods have emerged incorporating finite element analysis to aid in describing complex geometric effects, while simultaneously visualizing the physicochemical properties of the described system [36-39]. Finite element incorporated numerical analysis has been successfully applied to such systems as nanoparticle translocation through a pore to simulate its resistive pulse response [40], metal nanoparticle impacts at a water|oil microITIES [41], as well as optimization of photo-ionic quantum yields at droplet ITIES [42].

In this work, FIB milling was applied to fabricate nanopore arrays in a hexagonal layout, which enabled formation of nanoITIES with constant pore-to-pore distance within each array. The effect of separation distances on ion diffusion was investigated by ion-transfer voltammetry *via* experiments and computational simulations using finite element analysis in a 3-dimensional geometry. It was found that the design criterion for square nanoarrays of $r_c/r_a \geq 56$ [28] is not sufficient to achieve independent diffusion within hexagonal array nanoITIES, while $r_c/r_a \geq 96$ is required to obtain maximum performance of nanoarrays in the hexagonal arrangement, which provides a basis for design and development of nanodevices with high efficiency.

2. Materials and methods

2.1. Experimental

Fabrication of nanopore arrays in silicon nitride (SiN) membranes (SIMPore Inc.) was undertaken by a dual beam focused ion beam-scanning electron microscope (FIB-SEM) instrument (LYRA3, Tescan, Brno,

Czech Republic). SEM imaging of the prepared arrays and measurement of geometric parameters (pore radius r_a, pore centre-to-centre separation distance r_c) was performed using a Zeiss Neon 40EsB (Carl Zeiss Nano Technology Systems, Oberkochen, Germany). The SiN membrane thickness was 50 nm, and all arrays studied were 10 x 10 pore arrays in hexagonal arrangement. Ion transfer electrochemistry experiments were implemented by attaching the fabricated SiN membranes to borosilicate glass tubes with a silicone sealant and placing the organic phase inside the tube so as to fill the pores in the membrane. Then the assembly was placed into a beaker containing the aqueous phase and the cell completed by insertion of a silver/silver chloride electrode into the aqueous phase and a silver wire pseudo-reference electrode directly into the organic phase. The aqueous phase electrolyte was 10 mM lithium chloride, spiked with tetrapropylammonium chloride (TPrACl) at different concentrations. The organic phase electrolyte was 10 mM tetradodecylammonium tetrakis(4-chlorophenyl)borate (ETH 500). All reagents were purchased from Sigma-Aldrich and used as received. Voltammetric experiments were implemented with an Autolab PGSTAT 302N with ECD module (Metrohm, The Netherlands) in two-electrode mode. All voltammograms were recorded as cyclic voltammograms, but the forward scans were employed for analysis.

2.2. Simulations

Computational simulations incorporating 3-dimensional geometries were employed to describe mass transport effects associated with ion transfer at hexagonal nanopore arrays of varying r_c/r_a configurations using COMSOL Multiphysics version 5.5 employing finite element analysis (FEA). For simplicity, 3D simulations incorporated only Fickian diffusion and did not include capacitive or migration effects. Fick's 2nd law in 3-dimensional Cartesian coordinates is:

$$-\frac{\partial J_{i^z,\alpha}(x,y,z,t)}{\partial t} = D_{i^z,\alpha}\nabla^2 c_{i^z,\alpha}$$
$$\frac{\partial c_{i^z,\alpha}(x,y,z,t)}{\partial t} = D_{i^z,\alpha}\left(\frac{\partial^2 c_{i^z,\alpha}(x,y,z,t)}{\partial x^2} + \frac{\partial^2 c_{i^z,\alpha}(x,y,z,t)}{\partial y^2} + \frac{\partial^2 c_{i^z,\alpha}(x,y,z,t)}{\partial z^2}\right) \quad [1]$$

where $D_{i^z,\alpha}$ and $c_{i^z,\alpha}$ are the diffusion coefficient and concentration of species *i* of charge *z* in phase *α* (either water, w, or oil, o). $D_{\mathrm{TPrA^+},w} \approx D_{\mathrm{TPrA^+},o} \approx D_{\mathrm{TPrA^+}}$ = 7.5 × 10^{-6} cm^2 s^{-1} was chosen to approximate the diffusion of tetrapropylammonium ($TPrA^+$) [43]. Initial bulk aqueous and oil phase concentrations of $TPrA^+$ were $c_{\mathrm{TPrA^+},w}$ = 100 and $c_{\mathrm{TPrA^+},o}$ = 0 µmol L^{-1}, respectively. Simple ion transfer of $TPrA^+$ at the ITIES housed within or at the surface of each nanopore was performed using Butler-Volmer kinetics according to the reaction in eq. 2; k_f and k_b are the rates of the forward and reverse processes described by equations 3 and 4, respectively.

$$TPrA_w^+ \underset{k_b}{\overset{k_f}{\rightleftarrows}} TPrA_o^+ \quad [2]$$

$$k_f = k^o \exp\left[(1-\alpha) f\left(\Delta_o^w\phi - \Delta_o^w\phi^{o'}\right)\right] \quad [3]$$

$$k_b = k^o \exp\left[-\alpha f\left(\Delta_o^w\phi - \Delta_o^w\phi^{o'}\right)\right] \quad [4]$$

where $k°$, α, $\Delta_o^w\phi$, and $\Delta_o^w\phi°'$ are the standard rate constant (1 cm s^{-1}), the transfer coefficient (0.5), the applied Galvani potential difference across the interface, and the formal ion transfer potential of $TPrA^+$ (0.15 V), respectively. Parameter f=F/(RT), within which F is Faraday's constant (96485.33 C mol^{-1}), R is the universal gas constant (8.314 J mol^{-1} K^{-1}), and T is temperature (298.15 K). $\Delta_o^w\phi$ was applied via eq. 5 in time-dependent mode where t is time, $\Delta_o^w\phi_i$ is the initial potential, and v is the scan rate equal to 0.005 V s^{-1} employed throughout, unless otherwise stated.

$$\Delta_o^w\phi = \Delta_o^w\phi_i + vt \qquad [5]$$

Ion transfer current was determined by integrating the flux of $TPrA^+$ across all of the ITIES surface boundaries through:

$$I = z_i F \int D_{i^z,\alpha} \nabla^2 c_{i^z,\alpha} \qquad [6]$$

Figure 1 illustrates one of the 3D nanopore array geometries employed. For simplicity, each nanopore is considered to be cylindrical; however, it is recognized that FIB milling will generate a conical-shaped pore [44].

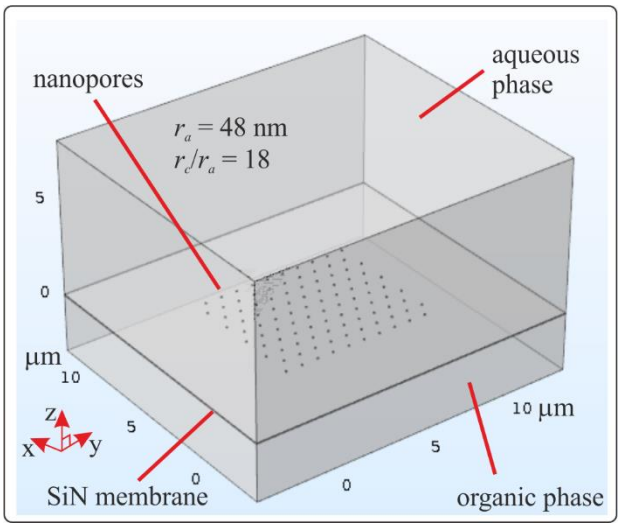

Figure 1. 3D simulation geometry for the 10 × 10 nanopore array with r_a = 48 nm and r_c/r_a = 18. The SiN membrane thickness was 50 nm, while the organic and aqueous phases were simulated to a height of 3 and 8 µm, respectively. Mirroring the experimental setup, the organic phase fills the nanopores so that the ITIES is located on the aqueous side of the membrane. The SiN boundary layer on either side of the membrane and along the inside surface of the pores was considered insulating. The external boundaries of the aqueous and organic phases were a continuous-concentration source/open boundary.

3. Results and Discussion

Figure 2A – F shows the SEM images of six nanopore arrays produced by FIB milling of SiN membranes. All arrays contain 10 x 10 pores in hexagonal arrangement, with approximately equal r_a and with r_c/r_a of 18 (A), 38 (B), 59 (C), 72 (D), 96 (E) and 118 (F). Figure 2G summarises the geometric characteristics of the arrays extracted from these images. The r_a (right Y axis) and r_c/r_a (left Y axis) values within each design had a small dispersion, with relative standard deviations less than 7% (n = 7) and 8% (n = 7), respectively, which is satisfactory for practical experiments.

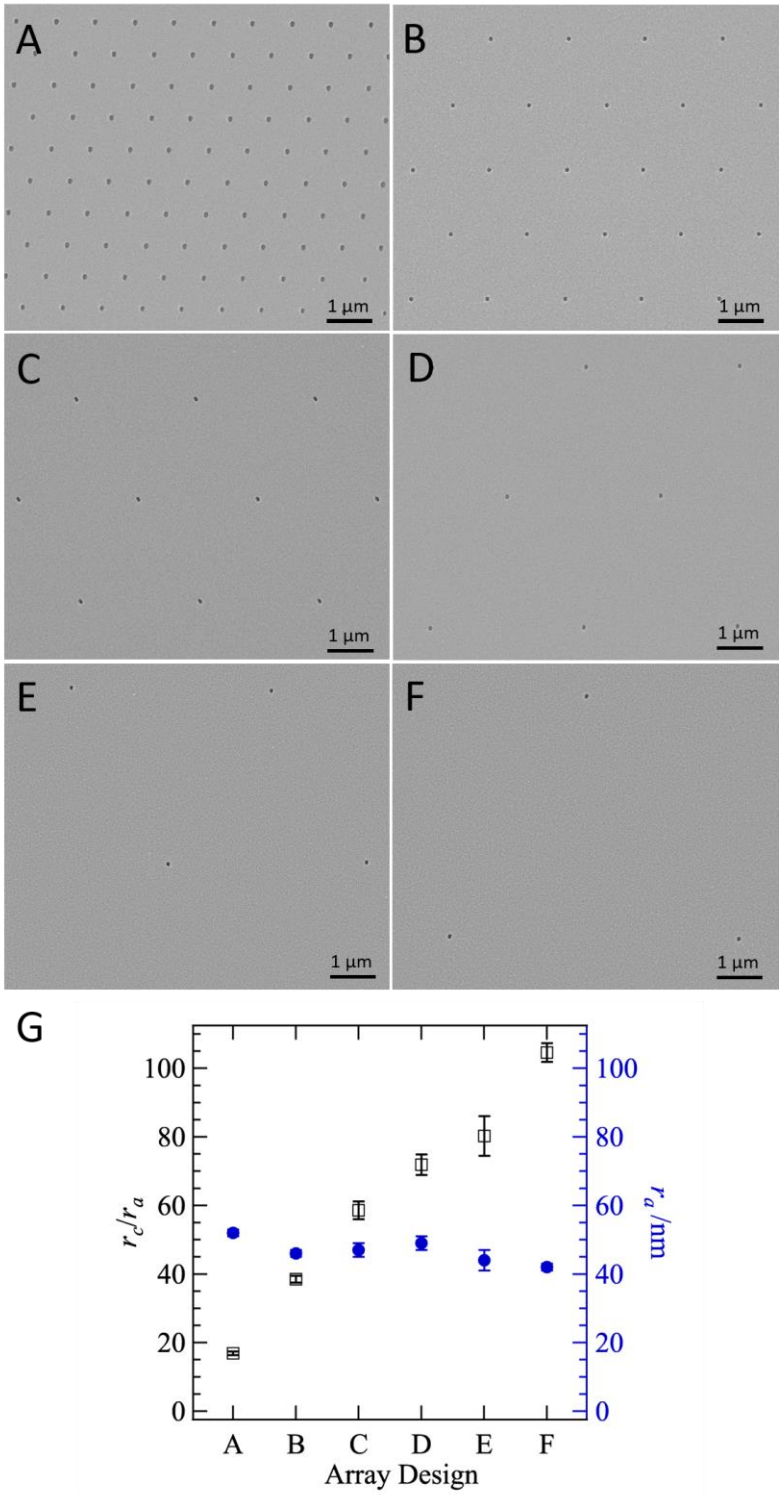

Figure 2. SEM images of nanopore arrays with r_c/r_a of 18 (A), 38 (B), 59 (C), 72 (D), 96 (E) and 118 (F). (G) The r_c/r_a (closed symbol, left Y axis) and r_a (open symbol, right Y axis) measured from the corresponding arrays in A-F.

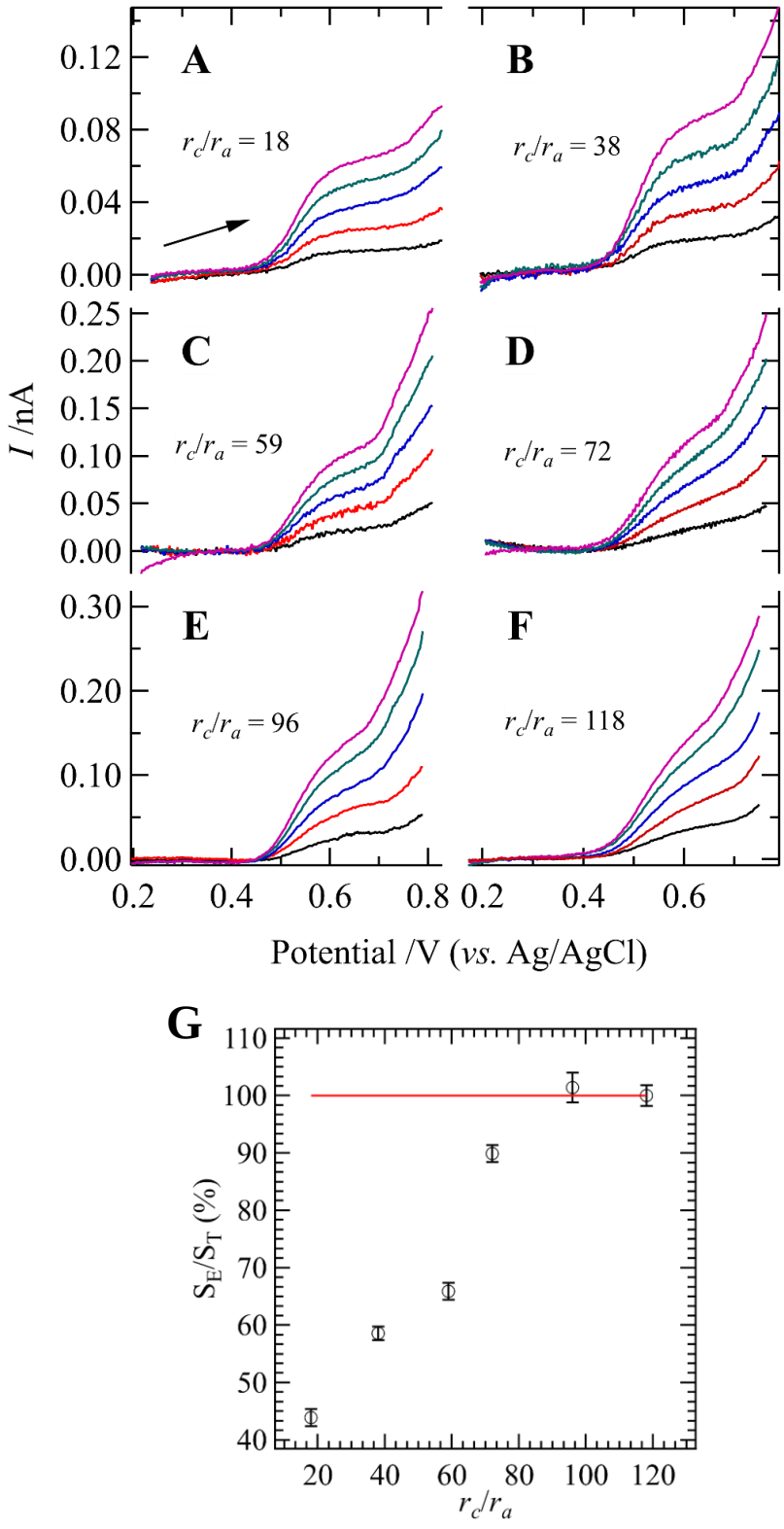

Figure 3. Background-subtracted forward-scan voltammograms of 20, 40, 60, 80 and 100 µM $TPrA^+$ transfer across the nanoITIES arrays with r_c/r_a of 18 (A), 38 (B), 59 (C), 72 (D), 96 (E) and 118 (F); scan rate, 5 mV s^{-1}. (G) Effect of r_c/r_a (18, 38, 59, 72, 96 and 118) on the experimental calibration plot slope (S_E) as a percentage of the theoretical calibration plot slope (S_T) for $TPrA^+$ transfer across the arrays of nanoITIES. Error bars are ±1 standard deviation based on the standard deviation of the slope.

Electrochemical characterisation of these arrays were implemented by detecting the current response for $TPrA^+$ transfer across the arrayed nanoITIES formed at the SiN membranes. Figure 3A – F shows the background-subtracted voltammograms for five concentrations (20, 40, 60, 80 and 100 μM) of $TPrA^+$ at each of the nanoITIES array designs. Note that cyclic voltammograms were recorded experimentally (see Figure S1) but for simplicity only the forward scan current is discussed in the following sections. It can be observed that the analyte commenced transfer from the water to organic phase at 0.45 V. The current increased steadily until a "sloping steady-state" current was reached in the diffusion-limited region, which is in good agreement with previously reported nanoITIES arrays [18, 45, 46]. In order to investigate the impact of different hexagonal nanoITIES array designs on the ion transfer current, the experimental and theoretical slopes of the calibration curves were systematically compared. Herein, an initial sloping steady-state current plateau reached at 0.65 V was determined as the experimental limiting current to evaluate the experimental slopes (S_E). Assuming that each nanoITIES behaves like an inlaid disk electrode, the theoretical slopes (S_T) can be calculated with the re-arranged Saito-Soos equation [47, 48],

$$S_T = 4|z|F D_{\mathrm{TPrA}^+} r_a N_p \qquad [7]$$

where S_T is the slope of the calibration curve obtained from the theoretical limiting currents (i_{ss}) plotted versus the concentrations of $TPrA^+$ (c_{TPrA^+}), r_a is the mean pore radius and N_p is the number of pores used to form the nanoITIES array. The diffusion coefficient for $TPrA^+$ in water (w) and oil (o) was considered equal, i.e., $D_{\mathrm{TPrA}^+,w} \approx D_{\mathrm{TPrA}^+,o} \approx D_{\mathrm{TPrA}^+} = 7.5\times10^{-6}$ cm^2 s^{-1} [43]. In this work, z=1 and N_p=100 were employed for all arrays, while the mean r_a of each array was used to calculate the theoretical slope for that array.

Figure 3G shows the effect of r_c/r_a varying from 18 to 118 on the experimental slope as a percentage of the theoretical slope (S_E/S_T) for $TPrA^+$ transfer across the hexagonal arrays of nanoITIES, i.e., a S_E/S_T value of 100% indicates perfect agreement between the expected (theoretical) slope and the experimental slope. It indicates that the experimental current is less than half of the theoretical current when r_c/r_a=18, which can be attributed to the strong overlap of diffusion zones at this low pore-to-pore separation. However, the S_E/S_T value approached the theoretical value as the r_c/r_a increased to 38, 59, 72, 96 and 118, which suggests that diffusion zone overlap is minimised and eventually eliminated as the pore-to-pore separation is increased. Interestingly, the current measured at the hexagonal array with r_c/r_a of 59, which is the design criterion for a square array to achieve independent diffusion [24, 28], is only 66±2% of the theoretical value. Instead, 101±3% of the theoretical current was achieved when r_c/r_a was increased to 96, which showed that independent radial diffusion occurred to each nanointerface in the hexagonal array. It means a larger pore-to-pore separation was required to eliminate diffusion zone overlap at nanoITIES arrays in hexagonal format compared with that in square format, which can be attributed to the different diffusion domains of these two array designs [22].

As described by Godino *et al.* [27], the interplay between the diffusion layer thickness (δ), nanopore radius (r_a), and separation distance between elements of an array (r_c) results in a relationship that can be described by four regimes [22]. Put simply, these transition between a regime in which the nanopores are well separated and experience independent radial diffusion at each pore, through an intermediary regime, into one in which there is extensive diffusional overlap. In the latter, the nanoarray behaves more like a single microITIES. The impact of nanoITIES separation distances was also investigated by the dimensionless scan rate parameter put forward by Guo and Lindner [24]. In this parameter, described by equation 8,

$$V = \frac{zF}{RT} \cdot \frac{v r_a}{D_{TPrA+}} \qquad [8]$$

V is the dimensionless scan rate, v is the experimental scan rate, and the other parameters are as already defined. Guo and Lindner [24] described five diffusion zones which can be selected based on combination of experimental and array design parameters. Zones III and IV describe totally independent radial diffusion and a combination of partially-radial and partially-linear diffusion, respectively. Based on that model, zone III is the sought-after condition where totally independent radial diffusion occurs at each element of the array. Using the design and experimental parameters employed here (i.e., typical pore radius used to form the

nanoITIES of 48 nm, diffusion coefficient of 7.5 x 10^{-6} cm^2 s^{-1} [43] and scan rate of 5 mV s^{-1}), a dimensionless scan rate of 1.5 x 10^{-7} is obtained. Based on the zone diagram in figure 3 of Guo and Lindner [24], five of the six arrays (B, C, D, E, F) studied here are in zone IV (partial radial and partial linear diffusion) and one array (A) is in zone V (linear diffusion).

To investigate further the diffusion characteristics at hexagonal patterned nanopore arrays, a 3D simulation was developed that incorporated all 100 nanopores used experimentally. The 3D approach has the advantage of observing simultaneously the diffusion regimes of nanopores positioned well within the array and those on the periphery which are less susceptible to diffusional overlap.

FEA simulations employed a tetrahedral mesh that was refined for the r_c/r_a = 118 case where the simulation was assumed to experience the lowest degree of diffusional overlap between pores and, therefore, highest agreement with eq. 7; element size was optimized to be 5 nm at each pore interface. The mesh size was decreased until the simulated linear sweep voltammograms (LSVs) steady state current varied by <0.1 pA (*i.e.* <~0.07% error) from the calculated value of 139 pA determined using eq. 9, which is similar to eq. 7, and describes the steady-state current (i_{ss}) at a micro/nano array [47, 48].

$$i_{ss} = 4|z|FD_{\mathrm{TPrA^+}} r_a N_p c_{\mathrm{TPrA^+}} \qquad [9]$$

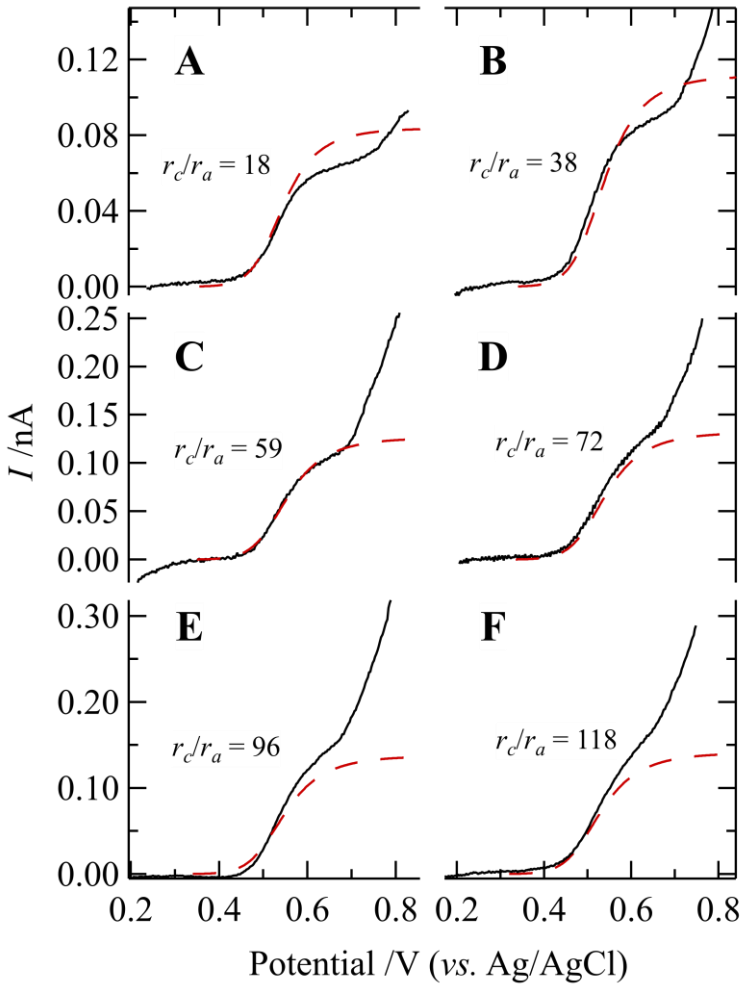

Figure 4. Comparison of background-subtracted experimental voltammograms with voltammograms obtained from simulations for 100 µM $TPrA^+$ transfer across the nanoITIES arrays with r_c/r_a of 18 (A), 38 (B), 59 (C), 72 (D), 96 (E) and 118 (F); scan rate, 5 mV s^{-1}.

Figure 4 shows simulated LSVs based on average nanoITIES dimensions in comparison to the background-subtracted experimental forward scans of cyclic voltammograms. Simulated LSVs show good agreement with the experimental voltammograms at low potentials during the onset of ion transfer;

however, there is a discrepancy at higher potentials, indicative of background electrolyte transfer, and which is at least qualitatively related to the array design parameter r_c/r_a.

Figure 5A shows simulated voltammograms for different values of the pore-pore separation ratio, r_c/r_a, and clearly indicates that as the pores forming the nanoITIES are placed further apart, the current increases, as expected. Figure 5B shows the plot of the ratio of simulated to theoretical current obtained using i_{ss} from the simulated voltammograms as a function of the separation ratio at a single concentration of analyte. These data follow the same trend as the experimental data (Figure 3G); however, at lower r_c/r_a values the simulated response is closer to the theoretical value (eqn 9) than are the experimental data. The differences between the experimental and simulated values may have a contribution from migration effects, which are not taken into account in the simulation model in which only Fick's laws of diffusion were used. On the other hand, it has been shown that migration does not play a role until the device/electrode sizes are in the 10 nm range [25, 49]. For illustrative purposes, the concentration profiles formed around these nanoITIES are shown in Figure 6 for two situations – arrays with more closely-arranged pores and arrays with more widely arranged pores. The concentration profiles around the closely spaced array (Figure 6A) indicate the formation of a single radial diffusion profile around the entire array, as discussed by Godino et al [27], while the profiles in Figure 6B indicate formation of independent diffusion profiles at each nanoITIES in the array.

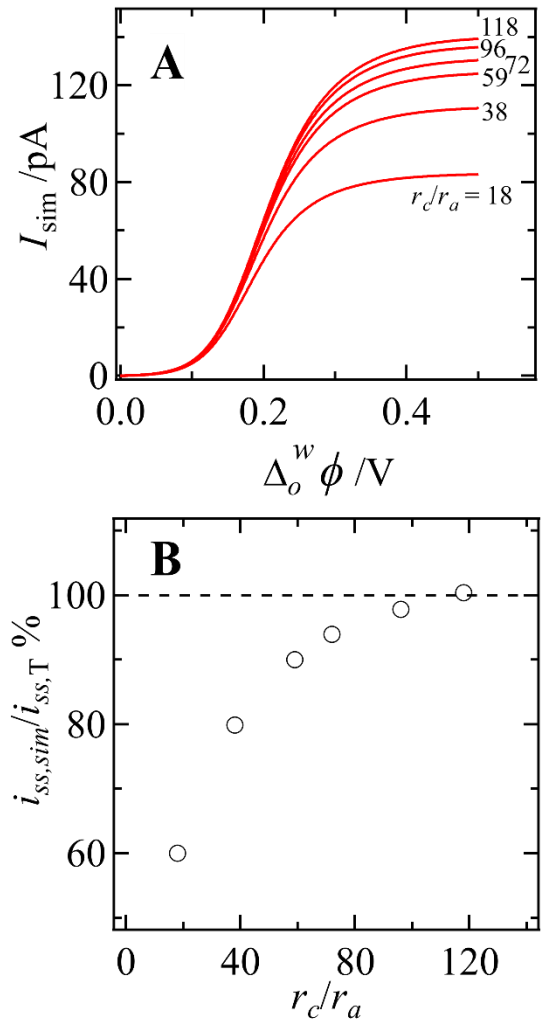

Figure 5. (**A**) Simulated LSVs (I_{sim} = simulated current) for varying r_c/r_a from 18 to 118 as indicated, and (**B**) a plot of the ratio of simulated steady state currents ($i_{ss,sim}$) in A to the theoretical current ($i_{ss,T}$, equation 9) versus r_c/r_a for the hexagonal arrays. Simulations were performed using the geometry described in Figure 1 at a scan rate of 0.005 V s^{-1} with $c_{TPrA^+,w}$ = 100 and $c_{TPrA^+,o}$ = 0 µmol L^{-1}.

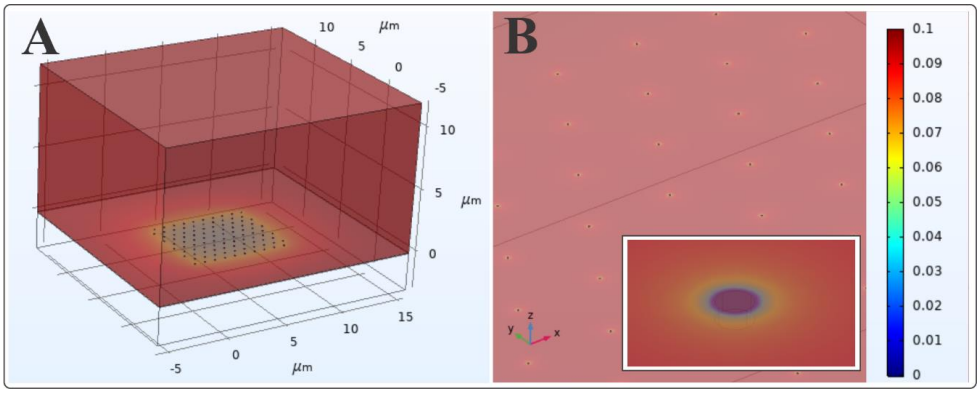

Figure 6. 3D concentration profiles of $TPrA^+$ in the aqueous phase at r_c/r_a equal to 18 (**A**) and 118 (**B**). (B) has been magnified to illustrate the concentration profile around the pores; inset is the concentration profile at a single pore for r_c/r_a = 118. Concentration scale at right is in mmol L^{-1}.

Based on our previous work [50], square patterned nanoarrays required an r_c/r_a ratio of ca. 56 to exhibit voltammetry consistent with independent radial diffusion to each nanoITIES or more accurately ca. 95% of the theoretical value; however, for the hexagonal patterned arrays shown in this work, an r_c/r_a ratio of 72 is needed to achieve a current that is ca. 94% of the theoretical current. This difference is likely due to the way that r_c is determined in both cases and the overall geometry of the nanoITIES positions. For the hexagonal case (Figure 7A), each element within the array has six equidistant adjacent elements. In the square patterned case (Figure 7B), r_c is only determined for the elements at cardinal positions to the central one and does not account for the elements positioned diagonally (indicated in the figure as having a separation distance of r_c^*). For example, if r_c = 1 μm, then $r_c^* = \sqrt{2}$ μm or ca. 1.4-times further way then elements located cardinally. As r_c/r_a increases, the diagonally positioned nanoITIES would present less interference to the central nanoITIES and thus less separation is required to elicit a radial diffusion regime at the central nanoITIES in the square patterned array versus the hexagonal array.

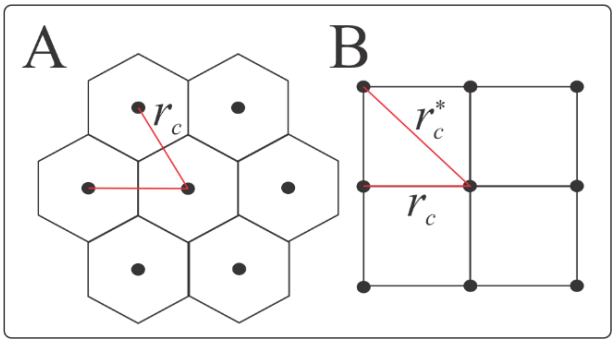

Figure 7. Hexagonal (A) versus square (B) patterned array geometries.

4. Conclusions

Ionic diffusion at hexagonal arrays of nanoITIES with different r_c/r_a ratios were studied via electrochemical experiments and computational simulations. It was found that the previously reported design criterion for nanoITIES arrays to achieve independent diffusion, which is $r_c/r_a \geq 56$, does not apply to the nanoITIES arrays in hexagonal arrangement, indicating the ion-transfer behaviours at nanoITIES arrays are not only dependent

on the r_c/r_a, but also influenced by design features of the nanoarrays that form the interfaces. At hexagonal nanoITIES arrays, the ratio $r_c/r_a \geq 96$ is required to achieve independent radial diffusion, which was in agreement with the simulated results. Hexagonal nanoarrays are more promising for the development of nanodevices, since the separation that determines the ionic diffusion mode is the same for all nanoITIES within the array; in contrast, in square arrays, the pores separated diagonally are further away, leading to inconsistent pore-to-pore distance. Therefore, the results are of importance for design of advanced nanoarray-based systems to achieve maximum performance. For analytical or sensor applications of nanoITIES arrays, the use of more sensitive instrumentation and/or arrays larger than 10 x 10 as used here can be anticipated.

5. Supplementary Materials

File containing Figure S1 cyclic voltammograms and associated text.

6. Acknowledgements

This work was supported by the Australian Research Council (DP130102040), the Natural Science and Engineering Research Council of Canada (Discovery Grant #006074-2019), Memorial University of Newfoundland, Science Foundation Ireland (Grant no. 13/SIRG/2137), the European Research Council (Starting Grant, Agreement no. 716792), and James Cook University. The authors acknowledge the use of equipment, scientific and technical assistance of the John de Laeter Centre, Curtin University, which has been partially funded by the University and by the State and Commonwealth Governments.

7. References

[1] Z. Samec, Electrochemistry at the interface between two immiscible electrolyte solutions, Pure and Applied Chemistry 76(12) (2004) 2147-2180.
[2] H.H. Girault, Electrochemistry at Liquid-Liquid Interfaces, in: A.J. Bard, C.G. Zoski (Eds.), Electroanalytical Chemistry, A Series of Advances, Vol 23, Dekker, New York, 2010, pp. 1-104.
[3] Z. Samec, E. Samcova, H.H. Girault, Ion amperometry at the interface between two immiscible electrolyte solutions in view of realizing the amperometric ion-selective electrode, Talanta 63(1) (2004) 21-32.
[4] G. Herzog, Recent developments in electrochemistry at the interface between two immiscible electrolyte solutions for ion sensing, Analyst 140(12) (2015) 3888-3896.
[5] J.A. Ribeiro, P.M.V. Fernandes, C.M. Pereira, F. Silva, Electrochemical sensors and biosensors for determination of catecholamine neurotransmitters: A review, Talanta 160 (2016) 653-679.
[6] S. Amemiya, J. Kim, A. Izadyar, B. Kabagambe, M. Shen, R. Ishimatsu, Electrochemical sensing and imaging based on ion transfer at liquid/liquid interfaces, Electrochimica Acta 110 (2013) 836-845.
[7] D.W.M. Arrigan, G. Herzog, M.D. Scanlon, J. Strutwolf, Bioanalytical Applications of Electrochemistry at Liquid-Liquid Microinterfaces, in: A.J. Bard, C.G. Zoski (Eds.), Electroanalytical Chemistry : A Series of Advances, Taylor and Francis, Hoboken, 2013, pp. 105-178.
[8] E. Goh, H.J. Lee, Applications of Electrochemistry at Liquid/Liquid Interfaces for Ionizable Drug Molecule Sensing, Rev. Polarogr. 62(2+3) (2016) 77-84.
[9] D.W.M. Arrigan, Y. Liu, Electroanalytical Ventures at Nanoscale Interfaces Between Immiscible Liquids, Annu. Rev. Anal. Chem. 9(1) (2016) 145-161.
[10] P.J. Rodgers, S. Amemiya, Cyclic Voltammetry at Micropipet Electrodes for the Study of Ion-Transfer Kinetics at Liquid/Liquid Interfaces, Anal. Chem. 79(24) (2007) 9276-9285.
[11] K. Rudnicki, L. Poltorak, S. Skrzypek, E.J.R. Sudhölter, Fused Silica Microcapillaries Used for a Simple Miniaturization of the Electrified Liquid–Liquid Interface, Anal. Chem. (2018).
[12] M.L. Colombo, J.V. Sweedler, M. Shen, Nanopipet-Based Liquid–Liquid Interface Probes for the Electrochemical Detection of Acetylcholine, Tryptamine, and Serotonin via Ionic Transfer, Anal. Chem. 87(10) (2015) 5095-5100.
[13] Y. Cheng, B. Su, Y. Shao, Studies on charge transfer across the micro-liquid/liquid interface supported at a double-barrel micropipette, 24 (2003) 1834-1837.

[14] A. Mastouri, S. Peulon, D. Farcage, N. Bellakhal, A. Chaussé, Perfect additivity of microinterface arrays for liquid-liquid measurements: Application to cadmium ions quantification, Electrochim. Acta 120 (2014) 212-218.
[15] R. Zazpe, C. Hibert, J. O'Brien, Y.H. Lanyon, D.W.M. Arrigan, Ion-transfer voltammetry at silicon membrane-based arrays of micro-liquid-liquid interfaces, Lab Chip 7(12) (2007) 1732-1737.
[16] E. Alvarez de Eulate, J. Strutwolf, Y. Liu, K. O'Donnell, D.W. Arrigan, An Electrochemical Sensing Platform Based on Liquid-Liquid Microinterface Arrays Formed in Laser-Ablated Glass Membranes, Analytical chemistry 88(5) (2016) 2596-604.
[17] M.D. Scanlon, J. Strutwolf, A. Blake, D. Iacopino, A.J. Quinn, D.W.M. Arrigan, Ion-Transfer Electrochemistry at Arrays of Nanointerfaces between Immiscible Electrolyte Solutions Confined within Silicon Nitride Nanopore Membranes, Anal. Chem. 82(14) (2010) 6115-6123.
[18] M. Sairi, N. Chen-Tan, G. Neusser, C. Kranz, D.W.M. Arrigan, Electrochemical Characterisation of Nanoscale Liquid|Liquid Interfaces Located at Focused Ion Beam-Milled Silicon Nitride Membranes, ChemElectroChem 2 (2015) 98-105.
[19] X. Huang, L.S.Q. Xie, X.Y. Lin, B. Su, Permselective Ion Transport Across the Nanoscopic Liquid/Liquid Interface Array, Analytical Chemistry 88(12) (2016) 6563-6569.
[20] L.S.Q. Xie, X. Huang, X.Y. Lin, B. Su, Nanoscopic liquid/liquid interface arrays supported by silica isoporous membranes: Trans-membrane resistance and ion transfer reactions, Journal of Electroanalytical Chemistry 784 (2017) 62-68.
[21] S. Fletcher, M.D. Horne, Random assemblies of microelectrodes (RAM™ electrodes) for electrochemical studies, Electrochem. Commun. 1(10) (1999) 502-512.
[22] T.J. Davies, R.G. Compton, The cyclic and linear sweep voltammetry of regular and random arrays of microdisc electrodes: Theory, J. Electroanal. Chem. 585(1) (2005) 63-82.
[23] T.J. Davies, S. Ward-Jones, C.E. Banks, J. del Campo, R. Mas, F.X. Muñoz, R.G. Compton, The cyclic and linear sweep voltammetry of regular arrays of microdisc electrodes: Fitting of experimental data, J. Electroanal. Chem. 585(1) (2005) 51-62.
[24] J. Guo, E. Lindner, Cyclic Voltammograms at Coplanar and Shallow Recessed Microdisk Electrode Arrays: Guidelines for Design and Experiment, Anal. Chem. 81(1) (2009) 130-138.
[25] E.J.F. Dickinson, R.G. Compton, Influence of the diffuse double layer on steady-state voltammetry, J. Electroanal. Chem. 661(1) (2011) 198-212.
[26] D. Krapf, B.M. Quinn, M.-Y. Wu, H.W. Zandbergen, C. Dekker, S.G. Lemay, Experimental Observation of Nonlinear Ionic Transport at the Nanometer Scale, Nano Lett. 6(11) (2006) 2531-2535.
[27] N. Godino, X. Borrisé, F.X. Muñoz, F.J. del Campo, R.G. Compton, Mass Transport to Nanoelectrode Arrays and Limitations of the Diffusion Domain Approach: Theory and Experiment, J. Phys. Chem. C 113(25) (2009) 11119-11125.
[28] Y. Liu, M. Sairi, G. Neusser, C. Kranz, D.W.M. Arrigan, Achievement of Diffusional Independence at Nanoscale Liquid–Liquid Interfaces within Arrays, Anal. Chem. 87(11) (2015) 5486-5490.
[29] Y. Liu, A. Holzinger, P. Knittel, L. Poltorak, A. Gamero-Quijano, W.D.A. Rickard, A. Walcarius, G. Herzog, C. Kranz, D.W.M. Arrigan, Visualization of Diffusion within Nanoarrays, Anal. Chem. 88(13) (2016) 6689-6695.
[30] P. Vazquez, G. Herzog, C. O'Mahony, J. O'Brien, J. Scully, A. Blake, C. O'Mathuna, P. Galvin, Microscopic gel–liquid interfaces supported by hollow microneedle array for voltammetric drug detection, Sensors and Actuators B: Chemical 201 (2014) 572-578.
[31] J. Strutwolf, M.D. Scanlon, D.W.M. Arrigan, Electrochemical ion transfer across liquid/liquid interfaces confined within solid-state micropore arrays – simulations and experiments, Analyst 134(1) (2009) 148-158.
[32] R. Cornut, C. Lefrou, New analytical approximations for negative feedback currents with a microdisk SECM tip, J. Electroanal. Chem. 604(2) (2007) 91-100.
[33] R. Cornut, C. Lefrou, New analytical approximation of feedback approach curves with a microdisk SECM tip and irreversible kinetic reaction at the substrate, J. Electroanal. Chem. 621(2) (2008) 178-184.
[34] E. Smirnov, P. Peljo, M.D. Scanlon, H.H. Girault, Gold Nanofilm Redox Catalysis for Oxygen Reduction at Soft Interfaces, Electrochim. Acta 197 (2016) 362-373.
[35] T. Kakiuchi, Electrochemical instability of the liquid｜liquid interface in the presence of ionic surfactant adsorption, J. Electroanal. Chem. 536(1) (2002) 63-69.

[36] D.J. Gavaghan, K. Gillow, E. Süli, Adaptive Finite Element Methods in Electrochemistry, Langmuir 22(25) (2006) 10666-10682.
[37] T. Nann, J. Heinze, Simulation in electrochemistry using the finite element method: Part 1: The algorithm, Electrochem. Commun. 1(7) (1999) 289-294.
[38] T. Nann, J. Heinze, Simulation in electrochemistry using the finite element method part 2: scanning electrochemical microscopy, Electrochim. Acta 48(27) (2003) 3975-3980.
[39] P. Peljo, M.D. Scanlon, T.J. Stockmann, Simulations employing finite element method at liquid|liquid interfaces, Current Opinion in Electrochemistry 7 (2018) 200-207.
[40] W.-J. Lan, D.A. Holden, B. Zhang, H.S. White, Nanoparticle Transport in Conical-Shaped Nanopores, Anal. Chem. 83(10) (2011) 3840-3847.
[41] T.J. Stockmann, L. Angelé, V. Brasiliense, C. Combellas, F. Kanoufi, Platinum Nanoparticle Impacts at a Liquid|Liquid Interface, Angew. Chem. Int. Ed. 56(43) (2017) 13493-13497.
[42] R. Bourdon, P. Peljo, M.A. Méndez, A.J. Olaya, J. De Jonghe-Risse, H. Vrubel, H.H. Girault, Chaotropic Agents Boosting the Performance of Photoionic Cells, J. Phys. Chem. C 119(9) (2015) 4728-4735.
[43] J. Langmaier, K. Stejskalová, Z. Samec, Evaluation of the standard ion transfer potentials for PVC plasticized membranes from voltammetric measurements, J. Electroanal. Chem. 496(1) (2001) 143-147.
[44] A. Holzinger, G. Neusser, B.J.J. Austen, A. Gamero-Quijano, G. Herzog, D.W.M. Arrigan, A. Ziegler, P. Walther, C. Kranz, Investigation of modified Nanopore Arrays by FIB/SEM Tomography, Faraday Discuss. 210 (2018) 113-130.
[45] M. Sairi, J. Strutwolf, R.A. Mitchell, D.S. Silvester, D.W.M. Arrigan, Chronoamperometric response at nanoscale liquid–liquid interface arrays, Electrochim. Acta 101(0) (2013) 177-185.
[46] M. Rimboud, R.D. Hart, T. Becker, D.W.M. Arrigan, Electrochemical behaviour and voltammetric sensitivity at arrays of nanoscale interfaces between immiscible liquids, Analyst 136(22) (2011) 4674-4681.
[47] Z.G. Soos, P.J. Lingane, Derivation of the Chronoamperometric Constant for Unshielded, Circular, Planar Electrodes1, J. Phys. Chem. 68(12) (1964) 3821-3828.
[48] Y. Saito, A Theoretical Study on the Diffusion Current at the Stationary Electrodes of Circular and Narrow Band Types, Rev. Polarogr. 15(6) (1968) 177-187.
[49] Y. Wang, D. Wang, M.V. Mirkin, Resistive-pulse and rectification sensing with glass and carbon nanopipettes, Proc. Math. Phys. Eng. 473(2199) (2017) 20160931.
[50] Y. Liu, J. Strutwolf, D.W.M. Arrigan, Ion-transfer voltammetric behavior of propranolol at nanoscale liquid-liquid interface arrays, Anal. Chem. 87(8) (2015) 4487-4494.